Laboratory Investigation (2020) 100:1280–1287
https://doi.org/10.1038/s41374-020-0475-7

ARTICLE

Characterization of pathological thyroid tissue using polarization-sensitive second harmonic generation microscopy

Danielle Tokarz[1] · Richard Cisek[1] · Ariana Joseph[1] · Sylvia L. Asa[2,3,4] · Brian C. Wilson[5,6] · Virginijus Barzda[7,8]

Received: 1 June 2020 / Revised: 7 July 2020 / Accepted: 9 July 2020 / Published online: 31 July 2020

Abstract

Polarization-sensitive second harmonic generation (SHG) microscopy is an established imaging technique able to provide information related to specific molecular structures including collagen. In this investigation, polarization-sensitive SHG microscopy was used to investigate changes in the collagen ultrastructure between histopathology slides of normal and diseased human thyroid tissues including follicular nodular disease, Grave's disease, follicular variant of papillary thyroid carcinoma, classical papillary thyroid carcinoma, insular or poorly differentiated carcinoma, and anaplastic or undifferentiated carcinoma ex vivo. The second-order nonlinear optical susceptibility tensor component ratios, $\chi^{(2)}{}_{zzz}{}'/\chi^{(2)}{}_{zxx}{}'$ and $\chi^{(2)}{}_{xyz}{}'/\chi^{(2)}{}_{zxx}{}'$, were obtained, where $\chi^{(2)}{}_{zzz}{}'/\chi^{(2)}{}_{zxx}{}'$ is a structural parameter and $\chi^{(2)}{}_{xyz}{}'/\chi^{(2)}{}_{zxx}{}'$ is a measure of the chirality of the collagen fibers. Furthermore, the degree of linear polarization (DOLP) of the SHG signal was measured. A statistically significant increase in $\chi^{(2)}{}_{zzz}{}'/\chi^{(2)}{}_{zxx}{}'$ values for all the diseased tissues except insular carcinoma and a statistically significant decrease in DOLP for all the diseased tissues were observed compared to normal thyroid. This finding indicates a higher ultrastructural disorder in diseased collagen and provides an innovative approach to discriminate between normal and diseased thyroid tissues that is complementary to standard histopathology.

Introduction

Thyroid cancers are the most common malignancy of the endocrine organs [1]. Papillary thyroid carcinoma is the most prevalent form, accounting for 85–90% of all thyroid cancer cases, while follicular thyroid carcinoma accounts for <10% [2, 3]. Both papillary and follicular thyroid carcinoma can spread to lymph nodes in the neck, but the latter is more likely to spread to distant organs such as the lungs and bones. Both papillary and follicular thyroid carcinomas are well-differentiated carcinomas composed of follicular epithelial cells, but their architecture is different. Well-differentiated thyroid carcinomas can be treated successfully if diagnosed early [4]. However, poorly differentiated and undifferentiated carcinomas have poor prognosis [5]. Although poorly differentiated insular and anaplastic carcinomas account for only <1–10% of thyroid cancer cases, they have more aggressive clinical behavior [6, 7]: the 10-year survival rates for patients

✉ Danielle Tokarz
danielle.tokarz@smu.ca

✉ Brian C. Wilson
brian.wilson@uhnresearch.ca

✉ Virginijus Barzda
virgis.barzda@utoronto.ca

[1] Department of Chemistry, Saint Mary's University, Halifax, NS, Canada

[2] University Health Network, University of Toronto, Toronto, ON, Canada

[3] University Hospitals Cleveland Medical Center, Cleveland, OH, USA

[4] Department of Pathology, Case Western Reserve University, Cleveland, OH, USA

[5] Princess Margaret Cancer Centre/University Health Network, Toronto, ON, Canada

[6] Department of Medical Biophysics, University of Toronto, Toronto, ON, Canada

[7] Department of Physics, University of Toronto, Toronto, ON, Canada

[8] Department of Chemical and Physical Sciences, University of Toronto Mississauga, Mississauga, ON, Canada

with insular and anaplastic carcinomas are 42% and 3%, respectively [8], but are 92% (Lorentz et al. 1994) and 80% (Lo et al. 1995) for papillary and follicular carcinomas, respectively.

Thyroid cancer diagnosis is typically confirmed by pathologists using stained biopsy or surgical resection tissue sections under bright-field microscopy. However, this is challenging and there is considerable intra- and inter-observer variability [9–11], but it is important to distinguish between the various carcinomas, since they are treated differently. Hence, additional information to aid diagnostic accuracy is required. During cancer initiation and progression, the extracellular matrix (ECM) is often deregulated and becomes disorganized. Thus, disease specificity and cancer diagnosis can be improved by identifying and quantifying this disorganization. This can be achieved by second harmonic generation (SHG) microscopy, since collagen, a non-centrosymmetric molecule that is the most abundant protein in the ECM, generates strong SHG signals without staining [12], allowing its density and spatial distribution to be imaged with little background signal. Quantitative results for automated pathology have been obtained from texture analysis of SHG intensity images of collagen in the ECM to distinguish between normal and diseased tissues including liver fibrosis [13, 14], human dermal disease [15], colon cancer [16], ovarian cancer [17], breast cancer [18], prostate cancer [19, 20], and malignant thyroid nodules [21] to name a few. However, these techniques are based on the macrostructural arrangement of collagen within the sample, and hence are sensitive once sufficiently large sample regions begin to show changes.

Additional collagen information can be extracted by using polarization-sensitive measurements, which reveal ultrastructural details of collagen in single laser focal volumes [22–31]. In the past decade, differences in collagen structure within normal and tumor tissues have been observed using polarization-sensitive SHG microscopy in several human tissues, including normal and malignant breast tissue [32–34], ovarian cancer [35, 36], colon cancer [37], non-small cell lung carcinoma [12], squamous-cell carcinoma [38], pancreatic ductal adenocarcinoma [39, 40] and well-differentiated thyroid carcinoma [41].

In this study, the polarization-sensitive SHG microscopy technique was used to investigate the difference in collagen structure polarization parameters between normal thyroid, benign disease, well-differentiated, poorly differentiated and undifferentiated thyroid carcinomas. The diseased tissues included: follicular nodular disease (FND, benign focal proliferation of the follicular epithelium), Grave's disease (benign diffuse hyperplasia), follicular variant of papillary thyroid carcinoma (FVPTC), classical papillary thyroid carcinoma (cPTC), insular or poorly differentiated carcinoma, and anaplastic or undifferentiated carcinoma. Several collagen structure polarization parameters were extracted, including $\chi^{(2)}{}_{zzz}'/\chi^{(2)}{}_{zxx}'$, $\chi^{(2)}{}_{xyz}'/\chi^{(2)}{}_{zxx}'$ and the degree of linear polarization (DOLP) of the SHG. The $\chi^{(2)}{}_{zzz}'/\chi^{(2)}{}_{zxx}'$ value is related to the distribution of collagen fibers within a focal volume, while the $\chi^{(2)}{}_{xyz}'/\chi^{(2)}{}_{zxx}'$ value is related to the chiral structure of collagen fibers within a focal volume, and both parameters are sensitive to the out-of-image-plane tilt angle. The DOLP is related to the disorder of collagen fibers within a focal volume. Significant differences in the mean $\chi^{(2)}{}_{zzz}'/\chi^{(2)}{}_{zxx}'$ and DOLP values were found between normal and most diseased tissues, suggesting a novel strategy to discriminate between normal and diseased tissues that is complementary to standard histopathology.

Materials and methods

Histology sample preparation

Normal and diseased histological sections of thyroid tissue were obtained according to an institutionally approved protocol (University Health Network, Toronto, Canada). Tissue sections of 5 μm thickness were cut from formalin-fixed, paraffin-embedded tissue blocks, mounted on glass slides and stained with hematoxylin and eosin (H&E). The staining was required so that the standard diagnosis could be performed by a pathologist to direct our imaging to regions of tissue with presence or absence of disease. The slides were imaged using a whole-slide scanner (ScanScope XT: Leica Biosystems, Germany) at 20× magnification.

In the resulting high-resolution bright-field microscopy images, the tissue architecture and cytology of cells were assessed by an expert pathologist (SLA). Subsequently, 110 μm × 110 μm regions of interest in each slide were scanned using polarization-in, polarization-out (PIPO) SHG microscopy [42]. Typically, 5–16 specimens were chosen for each condition (normal, FND, Graves', FVPTC, cPTC, insular, and anaplastic) by the pathologist SLA. For each specimen, sample regions that were clearly diagnosable were chosen for SHG analysis, and typically 1–8 were found in each specimen. Only fits with goodness of fit $R^2 > 0.8$ were used for subsequent analysis, hence the following number of scan regions per specimen were used: for normal thyroid tissue, five specimens were imaged. The number of areas imaged within the five specimens was: 8, 3, 2, 2, 1, respectively. For specimens with FND lesions we imaged ten specimens, the number of areas imaged within the ten specimens was: 1, 5, 2, 5, 1, 3, 1, 2, 3, 2, respectively. For Grave's disease, seven specimens were imaged, and the number of areas imaged within the seven specimens was: 4, 4, 4, 4, 1, 3, 2, respectively. For FVPTC tumors, sixteen specimens were imaged. The number of areas imaged within the sixteen specimens was: 1, 2, 4, 2, 4, 4, 1, 2, 1, 2, 1, 2, 2, 4, 4, 3, respectively. For cPTC tumors, eight specimens were imaged. The number of areas imaged within

the eight specimens was: 5, 7, 4, 7, 2, 1, 3, 3, respectively. For insular tumors, eight specimens were imaged. The number of areas imaged within the eight specimens was: 2, 1, 3, 4, 4, 2, 4, 4, respectively. For anaplastic tumors, four specimens were imaged. The number of areas imaged within the four specimens was: 4, 2, 7, 6, respectively. Two-tailed t tests were conducted to compare the different tissue classes, where each parameter was treated as an independent variable, with $p < 0.05$ considered statistically significant.

Nonlinear optical microscope setup

SHG imaging was performed using a custom-built Yb:KGW laser operating at 1028 nm, 14.3 MHz repetition rate and ~450 fs pulse duration [43] and coupled into a custom-built nonlinear optical microscope (Fig. 1), as described previously [44, 45]. Briefly, the laser beam was raster scanned at up to 10 frames per second using galvanometric scanning mirrors (VM1000, Cambridge Technology, USA) through a 0.75 numerical aperture (NA) air immersion objective lens (Plan-Apochromat 20×, Carl Zeiss AG, Germany) that does not alter the laser polarization. A custom-built 0.85 NA collection objective lens (Omex Technologies, USA) was used to collect SHG signal in transmission mode.

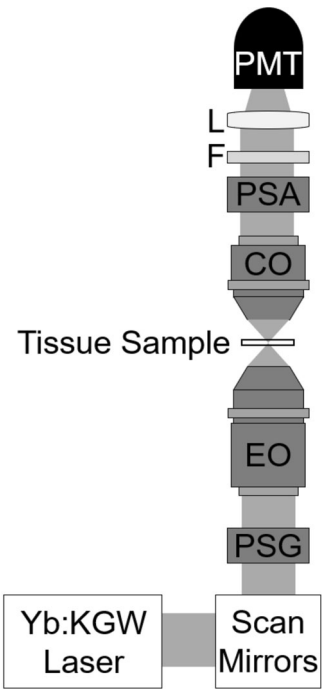

Fig. 1 A schematic of the nonlinear optical microscope. A polarization-state generator (PSG) is positioned before the excitation objective lens (EO) and the sample stage holding the tissue sample. After the collection objective lens (CO), a polarization-state analyzer (PSA) is present. The PSG consists of a fixed polarizer followed by a motorized half-wave plate while the PSA consists of a motorized polarizer. A filter (F) and lens (L) are placed before the photomultiplier tube (PMT) to ensure detection of second harmonic generation signal.

The SHG signal was collected using an interference filter centered at 514.5 nm with 10 nm bandwidth (F10-514.5, CVI Laser Optics, USA). Due to the intense excitation laser light, SHG imaging required additional filtering with a Schott color glass filter (BG39, CVI Laser Optics, USA). SHG signals were measured using single-photon-counting detector (H7421-40 Hamamatsu Photonics K.K., Japan).

The PIPO technique was used for polarization measurements of the SHG signals, as described previously [42]. Briefly, in order to rotate the incident laser polarization, a polarization-state generator (PSG) consisting of a stationary linear polarizer (IR 1100 BC4, Laser Components, Germany) followed by a motorized half-wave plate (532GR-42, Comar Optics Ltd, UK) was placed before the excitation objective lens. A polarization-state analyzer (PSA) consisting of a motorized linear polarizer (10LP-VIS-B, Newport Corporation, USA) was placed after the collection objective lens to measure the polarization of the SHG signal.

SHG images were recorded at 9 equidistant analyzer orientation angles of the PSA for each of 9 PSG half-wave plate angles. Additional images were obtained at reference polarizer and analyzer angles every 9 images to verify that the SHG intensity remained constant throughout the acquisition routine. A ~0.5 nJ pulse energy was used for PIPO SHG imaging.

Second-order nonlinear optical susceptibility ratio and degree of linear polarization

PIPO SHG measurements were used to determine the second-order nonlinear optical susceptibility tensor component ratio of collagen fibers within thyroid tissue as described previously [42, 46]. Briefly, a laboratory Cartesian coordinate system (XYZ) was used to express the principal propagation direction of the laser (Y) and the image plane (XZ). The average orientation of collagen fibers in a voxel was defined by the modified spherical angles δ and α. δ is defined as the average in-plane fiber orientation measured from the Z-axis, while α is defined as the out-of-plane tilt angle of the fiber.

By assuming C_6 symmetry, the SHG intensity can be described as a function of the laser electric field polarization orientation (θ) and the orientation of the analyzer (φ) [47]:

$$I_{2\omega} \propto \left| \begin{array}{c} \frac{\chi^{(2)}_{xxz'}}{\chi^{(2)}_{zxx'}} \sin(\varphi-\delta)\sin 2(\theta-\delta) + \cos(\varphi-\delta)\sin^2(\theta-\delta) \\ + \frac{\chi^{(2)}_{zzz'}}{\chi^{(2)}_{zxx'}} \cos(\varphi-\delta)\cos^2(\theta-\delta) \\ + 2\frac{\chi^{(2)}_{xyz'}}{\chi^{(2)}_{zxx'}} \cos(\varphi-\delta)\sin(\theta-\delta) \end{array} \right|^2, \quad (1)$$

where the primed second-order nonlinear optical susceptibility tensor components denote the molecular susceptibility projected onto the image plane. From Eq. (1), it is seen that three second-order nonlinear optical susceptibility tensor component ratios of an arbitrarily oriented collagen fiber can be deduced. The assumption that $\chi^{(2)}{}_{xxz}'/\chi^{(2)}{}_{zxx}'$ is equal to 1 was made for more accurate fitting and this assumption is valid to a good approximation, as shown by measurements of collagen in pig tendon using nonlinear Stokes-Mueller polarimetric microscopy [48].

The measured second-order nonlinear optical susceptibility tensor component ratios of the molecular susceptibility projected onto the image plane ($\chi^{(2)}{}_{zzz}'/\chi^{(2)}{}_{zxx}' = R$ and $\chi^{(2)}{}_{xyz}'/\chi^{(2)}{}_{zxx}' = C$) at an angle α is related to the molecular second-order nonlinear optical susceptibility tensor component ratios ($\chi^{(2)}{}_{zzz}/\chi^{(2)}{}_{zxx}$ and $\chi^{(2)}{}_{xyz}/\chi^{(2)}{}_{zxx}$) by [47]:

$$\begin{aligned}\frac{\chi^{(2)}_{zzz}{}'}{\chi^{(2)}_{zxx}{}'} &= \frac{\chi^{(2)}_{zzz}}{\chi^{(2)}_{zxx}}\cos^2\alpha + 3\sin^2\alpha = R \\ \frac{\chi^{(2)}_{xyz}{}'}{\chi^{(2)}_{zxx}{}'} &= \frac{\chi^{(2)}_{xyz}}{\chi^{(2)}_{zxx}}\sin\alpha = \mathrm{C}.\end{aligned} \tag{2}$$

At small α angles, R is representative of its molecular counterpart, while C is near 0.

In addition to measuring R and C, a third parameter, the degree of linear polarization (DOLP), was also measured using the following equation:

$$\mathrm{DOLP} = \frac{\sqrt{s_1^2 + s_2^2}}{s_0}. \tag{3}$$

The SHG polarization is described by Stokes parameters: s_0, s_1, and s_2 defined as: $s_0 = I_0 + I_{90}$, $s_1 = I_0 - I_{-90}$, and $s_2 = I_{45} - I_{-45}$, where I_φ is the SHG intensity at analyzer angle φ. DOLP measurements at 8 incident laser polarizations (0, 22.5, 45, 67.5, 90, 112.5, 135, and 157.5°) were averaged, where two DOLP calculations for each were averaged, one using measurements at analyzer angles 0, 45, 90, and 135° and the other at 22.5, 67.5, 112.5, and 157.5°.

Using custom MATLAB software (The Mathworks, Inc.), the PIPO SHG data were fit with Eqs. (1)–(3). Birefringence was neglected, since the tissue sections were thin (5 μm) [46].

Results

The top two rows in Fig. 2 show bright-field microscopy as well as typical SHG images of normal, hyperplastic (FND, Graves') and malignant (FVPTC, cPTC, insular, and anaplastic) thyroid tissues. These images were analyzed using both C_{6v} and C_6 symmetry. Using C_{6v} symmetry, the structural parameter, R, for each pixel was determined. Color-coded maps of the fitted R values for normal and diseased thyroid tissue samples are seen in Fig. 2, row 3. The graphs in row 4 are the corresponding frequency histograms of the R values, from which the mean R values and the full width at half maximum (FWHM) of the R distribution can be calculated by Gaussian fitting. The results are summarized in Table 1.

The mean R values in normal thyroid tissue were significantly smaller than in most pathological thyroid tissues, including FVPTC ($p < 0.05$) and cPTC ($p < 0.05$), consistent with previous data [41], as well as FND ($p < 0.001$), Grave's ($p < 0.01$) and anaplastic ($p < 0.02$). The exception was insular carcinoma, where the differences in the mean R values between normal and insular thyroid tissues have mean R values that differ by 0.01 from one another. Similarly, the mean R values in insular carcinoma were significantly smaller than in the other pathological thyroid tissues, including FND ($p < 0.001$), Graves' ($p < 0.01$), FVPTC ($p < 0.05$), and anaplastic carcinoma ($p < 0.02$). This is also seen visually in the color-coded maps of the fitted R values, where more blue and green pixels corresponding to lower R values are clearly seen in normal and insular carcinoma tissue (Fig. 2a3, f3), while more red pixels corresponding to higher R values are seen in the other tissues (Fig. 2b3–e3, g3).

The mean R values of FVPTC and cPTC tissues are not significantly different, varying by <0.01, but both FVPTC ($p < 0.05$) and cPTC ($p < 0.05$) tissues are significantly different from anaplastic carcinoma. However, due to a large standard deviation in the R values of anaplastic carcinoma, the mean R values of FND and Graves' tissues, which are slightly higher than in FVPTC and cPTC tissues, are not significantly different from anaplastic carcinoma. The mean R value of Graves' tissue is not significantly different from those of FVPTC and cPTC, but mean R value of FND tissue was significantly different from that of cPTC ($p < 0.05$).

The FWHM of the frequency histogram of normal thyroid tissue was generally larger than most of the abnormal tissues, including cPTC, insular carcinoma, FND and Graves' disease, indicating that these have a narrower collagen orientation distribution. However, this difference was only statistically significant for cPTC ($p < 0.05$), which had the smallest FWHM of all tissues. Significant differences in the FWHM were also found between diseased tissues, specifically between cPTC and anaplastic carcinoma ($p < 0.05$), the latter having the largest mean FWHM of all tissues. Similarly, the FWHM of FND tissue, which had a slightly higher mean R value than cPTC, also significantly differed from that of anaplastic carcinoma ($p < 0.05$).

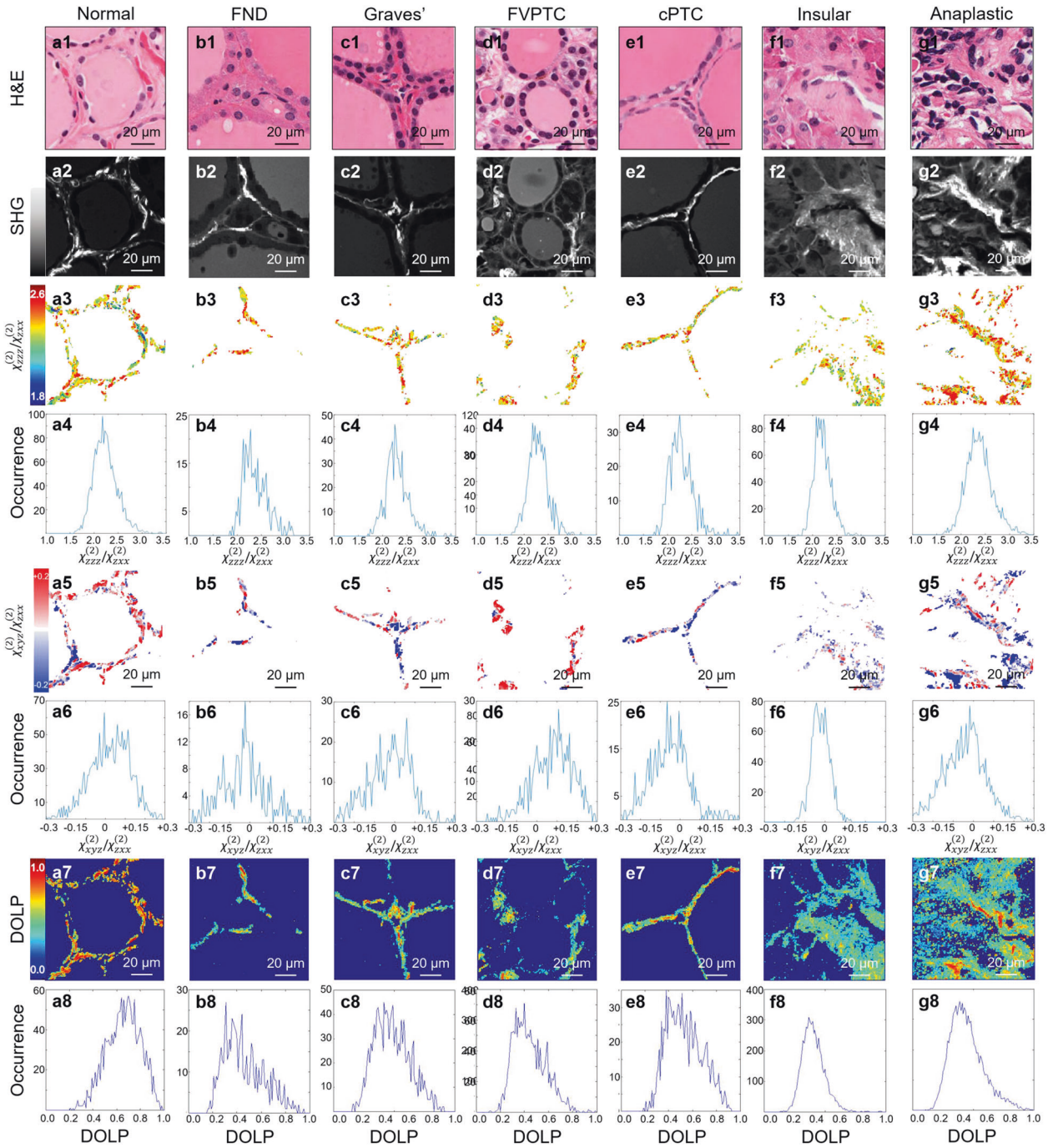

Fig. 2 PIPO SHG microscopy of normal and different pathological thyroid tissues. Bright-field microscopy (a1–g1) as well as PIPO SHG measurements (a2–g8) of collagen in normal (**a**) and pathological thyroid tissues (**b**–**g**): hyperplasia (FND (**b**) and Graves' (**c**)) and tumor (FVPTC (**d**), cPTC (**e**), Insular (**f**) and Anaplastic (**g**)). SHG intensity images (a2–g2) of selected regions are shown, together with color-coded maps of the fitted R values (a3–g3) assuming C_{6v} symmetry, and occurrence histograms of the R values (a4–g4). Color-coded maps of the fitted C values (a5–g5) and their occurrence histograms (a6–g6) assuming C_6 symmetry are also presented. Lastly, color-coded maps of the extracted DOLP values (a7–g7) and their occurrence histograms are displayed (a8–g8). The scale bar in the H&E images, the SHG intensity images and color-coded maps represents 20 μm.

Using C_6 symmetry, the chiral fitting component, C, for each pixel was additionally determined. Color-coded maps of the fitted C values for normal and diseased thyroid tissue samples are seen in row 5 of Fig. 2. The two colors indicate if the average tilt of the collagen fibers is above or below the imaging plane. The graphs in row 6 are the frequency histograms of the corresponding C values, the FWHM of which is related to the distribution of collagen tilt angles.

Table 1 *R*, *C*, and DOLP values (mean ± 1 standard deviation), assuming C_{6v} symmetry and C_6 symmetry for normal and pathological (FVPTC, cPTC, Insular, FND, Graves', and anaplastic) tissues.

Tissue	Samples (Areas)	*R* (C_{6v}) (FWHM)	*C* (FWHM)	DOLP
Normal thyroid	5 (16)	2.16 ± 0.05 (0.69 ± 0.02)	0.00 ± 0.04 (0.18 ± 0.03)	0.71 ± 0.08
FND	10 (25)	2.30 ± 0.06* (0.66 ± 0.09)	0.03 ± 0.05 (0.18 ± 0.10)	0.49 ± 0.13*
Graves'	7 (22)	2.25 ± 0.04* (0.67 ± 0.08)	0.00 ± 0.07 (0.19 ± 0.07)	0.47 ± 0.06*
FVPTC	16 (39)	2.24 ± 0.10* (0.71 ± 0.40)	0.01 ± 0.05 (0.20 ± 0.08)	0.43 ± 0.10*
cPTC	8 (32)	2.23 ± 0.07* (0.63 ± 0.07)*	−0.04 ± 0.04 (0.20 ± 0.08)	0.51 ± 0.10*
Insular	8 (34)	2.17 ± 0.06 (0.66 ± 0.09)	0.01 ± 0.04 (0.17 ± 0.04)	0.40 ± 0.04*
Anaplastic	4 (19)	2.42 ± 0.16* (0.83 ± 0.15)	0.00 ± 0.07 (0.16 ± 0.03)	0.47 ± 0.03*

The number of areas analyzed are given in brackets under "Samples." The full width at half maximum (FWHM) of the frequency histograms are given in brackets under the *R* and *C* values.

*Indicates statistically different from the corresponding normal thyroid tissue values ($p < 0.05$).

These maps visualize the distribution of the collagen polarity and/or the out-of-image-plane tilt angle. In addition, the molecular susceptibility of chiral components contributes to the *C* value distribution. The *C* values and the FWHM values for the normal thyroid tissue and all the pathological thyroid tissues studied were similar, as seen in the color-coded maps, where collagen fibers are similarly clustered into small positive- and negative-polarity regions.

The mean DOLP for normal thyroid tissue was significantly larger than those of all pathological tissues, including FVPTC ($p < 0.001$), cPTC ($p < 0.001$), FND ($p < 0.002$), Graves' ($p < 0.01$), insular ($p < 0.001$), and anaplastic carcinoma ($p < 0.001$). This is also apparent in the color-coded maps of the DOLP values (Fig. 2a7–g7), where normal tissue (Fig. 2a7) has more red pixels and the diseased tissues have more green and blue pixels (Fig. 2b7–g7). Amongst the diseased tissues, the DOLP for insular carcinoma, which had the lowest mean DOLP value and hence the most depolarized SHG, was significantly different than most of the other abnormal tissues, including FND ($p < 0.05$), Graves' ($p < 0.02$), cPTC ($p < 0.01$) and anaplastic carcinoma ($p < 0.01$), except for FVPTC which had a mean DOLP value that was only 0.03 higher.

Discussion

The observed increase in the mean *R* values for diseased thyroid tissues is consistent with previous studies in human lung [12], breast [33], and pancreas [40]. The values of *R* have also been investigated in other tissues of varying degree of disorder. Well-ordered collagen in the tibia [46] had a mean *R* value of ~1.1, compared with the theoretical maximum value of 3 (under the assumption that $\chi^{(2)}_{xxz}/\chi^{(2)}_{zxx} = 1$). Hence, increased *R* values in diseased tissues is attributed to increased disorder, which in turn may be attributed to variations in the amino acid content of the triple helices [46], the arrangement of the helices into fibrils, fibers and fascicles, and the distribution of fibrils, fibers and fascicles within the laser focal volume [12].

The fact that the average *C* value for normal tissue was not significantly different than that for diseased tissues is as expected, since the *C* values depend on the angle at which the tissue was sectioned, which was arbitrary from sample to sample. Further, the FWHM of the *C* values were also not significantly different in diseased tissues as compared to normal tissues. Previously, the FWHM of the *C* parameter showed variation between parenchymal pancreas tissue and tumor tissue [40]. This parameter is based on the intrinsic chirality of the collagen fibers pointing out of the image plane, and variations in it likely originate from different angular distributions of the collagen fibers. Hence, diseased thyroid tissue may have similar angular distributions of collagen fibers as normal thyroid, or, the angles of the fibers are not sufficiently pointing out of the image plane. To determine whether differentiation between thyroid tissues based on the average *C* values is possible, the absolute *C* values could be measured using the strategy by Golaraei et al. [48] where pig tendon at different sliced angles was measured, and the variation in *C* versus the angle was fitted to obtain the tissue absolute *C* value. However, this strategy may be complicated by the heterogeneous structure of diseased tissue regions.

The mean DOLP for normal thyroid tissue was significantly larger than that of all of the pathological tissues studied. Interestingly, insular carcinoma had the lowest mean DOLP value, indicating the most depolarized SHG. Again, this is not entirely unexpected, since one of the features of insular carcinomas is reduction of the normal stromal components and loss of adhesion by tumor cells [49]. It is, however, surprising that the value for FVPTC are markedly different from normal thyroid, which it resembles architecturally. This is an example of how PIPO SHG parameters may find application in resolving pathologic diagnostic controversies [9, 10].

To conclude, human thyroid tissue samples were successfully imaged by polarization-resolved SHG microscopy.

Using the *R* and DOLP polarization PIPO SHG parameters, normal thyroid tissue can be distinguished from a number of thyroid diseases. Hence, the determination of *R* and DOLP polarization SHG parameters can potentially be used to identify diseased thyroid tissue. While the most common challenge, to distinguish FVPTC from benign follicular lesions such as FND, is not particularly helpful, the data suggest that SHG microscopy may provide an ancillary tool to distinguish cPTC from Graves' disease and to identify dedifferentiation to insular carcinoma that may not be obvious in tumors that are predominantly differentiated carcinomas.

In this study, forward-scattered SHG signals from thin sections were collected for applicability in automated diagnosis of pathological samples. The technique might be applicable to live medical diagnosis if epi-detection of SHG signals is utilized as well as modeling and compensation of polarization scattering during reflections and the addition of a dichroic mirror is performed.

Acknowledgements This research was supported by the Natural Sciences and Engineering Research Council of Canada (NSERC RGPIN-2017-06923 and DGDND-2017-00099) and the Canadian Institutes of Health Research (CIHR) through a Collaborative Health Research Project (CHRP) grant (CPG-134752 and CHRPJ 462842-14). The authors thank the staff of the Advanced Optical Microscopy Facility at University Health Network for assistance with whole-slide scanning.

Compliance with ethical standards

Conflict of interest The authors declare that the research was conducted in the absence of any commercial or financial relationships that could be construed as a real or potential conflict of interest.

Publisher's note Springer Nature remains neutral with regard to jurisdictional claims in published maps and institutional affiliations.

References

1. American Cancer Society. Cancer facts & figures. Atlanta: American Cancer Society; 2019. https://www.cancer.org/content/dam/cancer-org/research/cancer-facts-and-statistics/annual-cancer-facts-and-figures/2019/cancer-facts-and-figures-2019.pdf.
2. Hundahl SA, Fleming ID, Fremgen AM, Menck HR. A National Cancer Data Base report on 53,856 cases of thyroid carcinoma treated in the U.S., 1985–1995. Cancer. 1998;83:2638–48.
3. LiVolsi VA, Asa SL. The demise of follicular carcinoma of the thyroid gland. Thyroid. 1994;4:233–6.
4. Schmidbauer B, Menhart K, Hellwig D, Grosse J. Differentiated thyroid cancer—treatment: state of the art. Int J Mol Sci. 2017;18:1292.
5. Justin EP, Seabold JE, Robinson RA, Walker WP, Gurll NJ, Hawes DR. Insular carcinoma: a distant thyroid carcinoma with associated iodine-131 localization. J Nucl Med. 1991;32:1358–63.
6. American Thyroid Association. Anaplastic thyroid cancer. Falls Church: American Thyroid Association; 2017. https://www.thyroid.org/wp-content/uploads/patients/brochures/anaplastic-thyroid-cancer-brochure.pdf.
7. Kazaure HS, Roman SA, Sosa JA. Insular thyroid cancer a population-level analysis of patient characteristics and predictors of survival. Cancer. 2012;118:3260–7.
8. Lam K, Lo C, Chan K, Wan K. Insular and anaplastic carcinoma of the thyroid: a 45-year comparative study at a single institution and a review of the significance of p53 and p21. Ann Surg. 2000;231:329–38.
9. Lloyd RV, Erickson LA, Casey MB, Lam KY, Lohse CM, Asa SL, et al. Observer variation in the diagnosis of follicular variant of papillary thyroid carcinoma. Am J Surg Pathol. 2004;28:1336–40.
10. Elsheikh TM, Asa SL, Chan JKC, DeLellis RA, Heffess CS, LiVolsi VA, et al. Interobserver and intraobserver variation among experts in the diagnosis of thyroid follicular lesions with borderline nuclear features of papillary carcinoma. Am J Clin Pathol. 2008;130:736–44.
11. Hirokawa M, Carney JA, Goellner JR, DeLellis RA, Heffess CS, Katoh R, et al. Observer variation of encapsulated follicular lesions of the thyroid gland. Am J Surg Pathol. 2002;26:1508–14.
12. Golaraei A, Cisek R, Krouglov S, Navab R, Niu C, Sakashita S, et al. Characterization of collagen in non-small cell lung carcinoma with second harmonic polarization microscopy. Biomed Opt Express. 2014;5:3562–7.
13. Gailhouste L, Grand YL, Odin C, Guyader D, Turlin B, Ezan F, et al. Fibrillar collagen scoring by second harmonic microscopy: A new tool in the assessment of liver fibrosis. J Hepatol. 2010;52:398–406.
14. Liu F, Chen L, Rao HY, Teng X, Ren YY, Lu YQ, et al. Automated evaluation of liver fibrosis in thioacetamide, carbon tetrachloride, and bile duct ligation rodent models using second-harmonic generation/two-photon excited fluorescence microscopy. Lab Investig. 2017;97:84–92.
15. Cicchi R, Kapsokalyvas D, De Giorgi V, Maio V, Van Wiechen A, Massi D, et al. Scoring of collagen organization in healthy and diseased human dermis by multiphoton microscopy. J Biophoton. 2010;3:34–43.
16. Zhuo S, Yan J, Chen G, Shi H, Zhu X, Lu J, et al. Label-free imaging of basement membranes differentiates normal, precancerous, and cancerous colonic tissues by second-harmonic generation microscopy. PLoS ONE. 2012;7:e38655.
17. Adur J, Pelegati VB, de Thomaz AA, Baratti MO, Andrade LALA, Carvalho HF, et al. Second harmonic generation microscopy as a powerful diagnostic imaging modality for human ovarian cancer. J Biophotonic. 2014;7:37–48.
18. Burke K, Smid M, Dawes RP, Timmermans MA, Salzman P, van Deurzen CHM, et al. Using second harmonic generation to predict patient outcome in solid tumors. BMC Cancer. 2015;15:929.
19. Ling Y, Li C, Feng K, Palmer S, Appleton PL, Lang S, et al. Second harmonic generation (SHG) imaging of cancer heterogeneity in ultrasound guided biopsies of prostate in men suspected with prostate cancer. J Biophoton. 2017;10:911–8.
20. Yuting L, Li C, Zhou K, Guan G, Appleton PL, Lang S, et al. Microscale characterization of prostate biopsies tissues using optical coherence elastography and second harmonic generation imaging. Lab Investig. 2018;98:380–90.
21. Hristu R, Eftimie LG, Stanciu SG, Tranca DE, Paun B, Sajin M, et al. Quantitative second harmonic generation microscopy for the structural characterization of capsular collagen in thyroid neoplasms. Biomed Opt Express. 2018;9:3923–36.
22. Freund I, Deutsch M, Sprecher A. Connective tissue polarity. Optical second-harmonic microscopy, crossed-beam summation, and small-angle scattering in rat-tail tendon. Biophys J. 1986;50:693–712.
23. Stoller P, Kim BM, Rubenchik AM, Reiser KM, Da Silva LB. Polarization-dependent optical second-harmonic imaging of a rat-tail tendon. J Biomed Opt. 2002;7:205–14.

24. Stoller P, Reiser KM, Celliers PM, Rubenchik AM. Polarization-modulated second harmonic generation in collagen. Biophys J. 2002;82:3330–42.
25. Stoller P, Celliers PM, Reiser KM, Rubenchik AM. Quantitative second-harmonic generation microscopy in collagen. Appl Opt. 2003;42:5209–19.
26. Williams RM, Zipfel WR, Webb WW. Interpreting second-harmonic generation images of collagen I fibrils. Biophys J. 2005;88:1377–86.
27. Erikson A, Ortegren J, Hompland T, Davies CD, Lindgren M. Quantification of the second-order nonlinear susceptibility of collagen I using a laser scanning microscope. J Biomed Opt. 2007;12:1–10.
28. Tiaho F, Recher G, Rouède D. Estimation of helical angles of myosin and collagen by second harmonic generation imaging microscopy. Opt Express. 2007;15:12286–95.
29. Nadiarnykh O, Campagnola PJ. Retention of polarization signatures in SHG microscopy of scattering tissues through optical clearing. Opt Express. 2009;17:5794–806.
30. Gusachenko I, Latour G, Schanne-Klein M-C. Polarization-resolved second harmonic microscopy in anisotropic thick tissues. Opt. Express. 2010;18:19339–52.
31. Su PJ, Chen WL, Chen YF, Dong CY. Determination of collagen nanostructure from second-order susceptibility tensor analysis. Biophys J. 2011;100:2053–62.
32. Ambekar R, Lau T-Y, Walsh M, Bhargava R, Toussaint KC. Quantifying collagen structure in breast biopsies using second-harmonic generation imaging. Biomed Opt Express. 2012;3: 2021–35.
33. Golaraei A, Kontenis L, Cisek R, Tokarz D, Done SJ, Wilson BC, et al. Changes of collagen ultrastructure in breast cancer tissue determined by second-harmonic generation double stokes-mueller polarimetric microscopy. Biomed Opt Express. 2016;7:4054–68.
34. Okoro C, Kelkar V, Sivaguru M, Emmadi R, Toussaint KC. Second-harmonic patterned polarization-analyzed reflection confocal microscopy of stromal collagen in benign and malignant breast tissues. Sci Rep. 2018;8:16243.
35. Campbell KR, Campagnola PJ. Assessing local stromal alterations in human ovarian cancer subtypes via second harmonic generation microscopy and analysis. J Biomed Opt. 2017;22:116008.
36. Campbell KR, Chaudhary R, Handel JM, Patankar MS, Campagnola PJ. Polarization-resolved second harmonic generation imaging of human ovarian cancer. J Biomed Opt. 2018;23: 066501.
37. Birk JW, Tadros M, Moezardalan K, Nadyarnykh O, Forouhar F, Anderson J, et al. Second harmonic generation imaging distinguishes both high-grade dysplasia and cancer from normal colonic mucosa. Dig Dis Sci. 2014;59:1529–34.
38. Hristu R, Stanciu SG, Tranca DE, Stanciu GA. Improved quantification of collagen anisotropy with polarization-resolved second harmonic generation microscopy. J Biophoton. 2017;10:1171–9.
39. Tokarz D, Cisek R, Golaraei A, Krouglov S, Navab R, Niu C, et al. Tumor tissue characterization using polarization-sensitive second harmonic generation microscopy. Proc. SPIE. 2015;9531: 95310C.
40. Tokarz D, Cisek R, Joseph A, Golaraei A, Mirsanaye K, Krouglov S, et al. Characterization of pancreatic cancer tissue using multiphoton excitation fluorescence and polarization-sensitive harmonic generation microscopy. Front Oncol. 2019;9:1–10.
41. Tokarz D, Cisek R, Golaraei A, Asa SL, Barzda V, Wilson BC. Ultrastructural features of collagen in thyroid carcinoma tissue observed by polarization second harmonic generation microscopy. Biomed Opt Express. 2015;6:3475–81.
42. Tuer AE, Krouglov S, Prent N, Cisek R, Sandkuijl D, Yasufuku K, et al. Nonlinear optical properties of type I collagen fibers studied by polarization dependent second harmonic generation microscopy. J Phys Chem B. 2011;115:12759–69.
43. Major A, Cisek R, Sandkuijl D, Barzda V. Femtosecond Yb:KGd (WO4)2laser with > 100 nJ of pulse energy. Laser Phys Lett. 2009;6:272–4.
44. Greenhalgh C, Prent N, Green C, Cisek R, Major A, Stewart B, et al. Influence of semicrystalline order on the second-harmonic generation efficiency in the anisotropic bands of myocytes. Appl Opt. 2007;46:1852–9.
45. Carriles R, Schafer DN, Sheetz KE, Field JJJ, Cisek R, Barzda V, et al. Invited Review Article: Imaging techniques for harmonic and multiphoton absorption fluorescence microscopy. Rev Sci Instrum. 2009;80:10364–71.
46. Tuer AE, Akens MK, Krouglov S, Sandkuijl D, Wilson BC, Whyne CM, et al. Hierarchical model of fibrillar collagen organization for interpreting the second-order susceptibility tensors in biological tissue. Biophys J. 2012;103:2093–105.
47. Golaraei A, Mirsanaye K, Ro Y, Krouglov S, Akens MK, Wilson BC, et al. Collagen chirality and three-dimensional orientation studied with polarimetric second-harmonic generation microscopy. J Biophoton. 2019;12:e201800241.
48. Golaraei A, Kontenis L, Mirsanaye K, Krouglov S, Akens MK, Wilson BC, et al. Complex susceptibilities and chiroptical effects of collagen measured with polarimetric second-harmonic generation microscopy. Sci Rep. 2019;9:124881–12.
49. Asa SL. Pathology survival guides, series 1, number 4: survival guide to endocrine pathology. Arlington: Innovative Science Press; 2020.